AIAA AVIATION Forum
June 25-29, 2018, Atlanta, Georgia
2018 Fluid Dynamics Conference

10.2514/6.2018-4035

Coherent-vorticity Preserving Large-Eddy Simulation of vortex rings under large perturbations

Z. Yu[1*] , J.-B. Chapelier[1] , C. Scalo[1]

[1]*School of Mechanical Engineering and Aeronautical Engineering, Purdue University, IN, USA*

In this paper, a numerical study of the dynamics of a perturbed vortex ring is conducted using Coherent-vorticity Preserving (CvP) Large-Eddy simulation[1] spanning circulation based Reynolds numbers Re_Γ in the range $7,000$-$700,000$. The vortex line corresponding to the vortex ring is defined using a parametric equation and perturbed with amplitude in the range of 10%-20% of the radius. Two types of perturbations are tested: sinusoidal (mode 10) and multi-mode. The Biot-Savart law is employed to define the corresponding induced velocity field. High levels of perturbation yield a transient bursting stage of the original vortex ring and the formation of a new one. The generation of dipoles and different types of vortex reconnection are accurately captured by the Cvp-LES. Vortex bursting is observed with large amplitude perturbations at the beginning of simulations. The ejection of dipoles at the inner and outer sides extracts vorticity from the vortex ring which loses its coherence immediately. Dipoles keep growing and the vortex core intensifies in the form of tangled vortex threads up to breakdown, leaving stable dipoles. Dipoles go through a viscous cancellation process and the vortex core is then slightly restored. The reasons of the persistence of coherent structures in all types of perturbations are analyzed. An axial flow, i.e. a flow along the vortex line is detected with multi-mode perturbation simulations, which is driven by the pressure gradient resulting from ejected dipoles and develops from nonuniform locations of pressure sources.

I. Introduction

Vortex rings are ubiquitous flow structures, which play a fundamental role in applications involving turbulent jets or rotor wake dynamics. Under certain sinusoidal perturbations of the vortex line, it has been shown analytically by Widnall & Sullivan (1973)[2] and Widnall, Bliss & Tsai (1974)[3] that the structure can become unstable. Further numerical studies conducted by Shariff et al.(1994) [4] at various Reynolds numbers reproduced the azimuthal instability and shed light on an amplification mechanism of mean swirl in the early nonlinear stage. Dazin et al.,[5,6] studied vortex ring instabilities using an experimental setup and observed a transfer of energy from the unstable modes to second azimuthal harmonics. Recently, a direct numerical simulation at Re_Γ=7500 was conducted by Bergdorf et al.,[7] investigating the origin and topology of the secondary vortex structures during the nonlinear stage of vortex ring decay.

In the present paper, we introduce a numerical setup to study numerically vortex ring instability under large perturbations. A vortex ring path is defined using a parametric equation, and the corresponding velocity field is found using the Biot-Savart law, coupled to a core smoothing function that allows to accurately define the size of the vortex core radius. A recently developed LES model,[1] which is able to capture accurately the dynamics of transitional vortical flows with at minimal grid resolution is employed.

*Corresponding author, yu754@purdue.edu

II. Methodology

A. Governing equations

The flow motion considered in the present study is assumed to be governed by the set of compressible Navier-Stokes equations:

$$\mathcal{NS}(\mathbf{w}) = \frac{\partial \mathbf{w}}{\partial t} + \boldsymbol{\nabla} \cdot [\mathbf{F}_{\mathrm{c}}(\mathbf{w}) - \mathbf{F}_{\mathrm{v}}(\mathbf{w}, \nabla \mathbf{w})] = \mathbf{0}, \tag{1}$$

where $\mathbf{w} = (\rho, \rho\mathbf{U}, \rho E)^{\mathrm{T}}$ is the vector of conserved variables ρ, $\mathbf{U}$ and E, density, velocity and total energy respectively, and $(\nabla \mathbf{w})_{ij} = \partial w_i / \partial x_j$ its gradient. The viscous and convective flux tensors $\mathbf{F}_{\mathrm{c}}, \mathbf{F}_{\mathrm{v}} \in \mathbb{R}^{5\times 3}$ read

$$\mathbf{F}_{\mathrm{c}} = \begin{pmatrix} \rho\mathbf{U}^{\mathrm{T}} \\ \rho\mathbf{U} \otimes \mathbf{U} + p\mathbf{I} \\ (\rho E + p)\mathbf{U}^{\mathrm{T}} \end{pmatrix}, \quad \text{and} \quad \mathbf{F}_{\mathrm{v}} = \begin{pmatrix} \mathbf{0} \\ \boldsymbol{\tau} \\ \boldsymbol{\tau} \cdot \mathbf{U} - \lambda \boldsymbol{\nabla} T^{\mathrm{T}} \end{pmatrix}, \tag{2}$$

where T is the temperature, p is the pressure, λ is the thermal conductivity of the fluid and $\mathbf{I} \in \mathbb{R}^{3\times 3}$ is the identity matrix. For a Newtonian fluid, we have

$$\boldsymbol{\tau} = 2\mu \mathbf{S}, \tag{3}$$

where μ is the dynamic viscosity and

$$\mathbf{S} = \frac{1}{2}\left[\nabla \mathbf{U} + \nabla \mathbf{U}^{\mathrm{T}} - \frac{2}{3}(\boldsymbol{\nabla} \cdot \mathbf{U})\mathbf{I}\right]. \tag{4}$$

The ideal gas law is considered for the closure of the system of equations, namely,

$$p = (\gamma - 1)\left(\rho E - \frac{1}{2}\rho \mathbf{U} \cdot \mathbf{U}\right), \tag{5}$$

where γ is the heat capacity ratio.

The LES equations are obtained by applying a low-pass filter to the Navier-Stokes equations.[8] The spatial filtering operator applied to a generic quantity ϕ reads

$$\overline{\phi}(\mathbf{x}, t) = g(\mathbf{x}) \star \phi(\mathbf{x}), \tag{6}$$

where $\star$ is the convolution product and $g(\mathbf{x})$ is a filter kernel related to a cutoff length scale $\overline{\Delta}$ in physical space.[9] The compressible case requires density-weighted filtering approaches. The density-weighted or Favre filtering operator is defined as

$$\widetilde{\phi} = \frac{\overline{\rho\phi}}{\overline{\rho}}. \tag{7}$$

In the present study, the compressible LES formalism introduced by Lesieur et al.[10–12] is adopted yielding the following set of filtered compressible Navier-Stokes equations:

$$\mathcal{NS}(\overline{\mathbf{w}}) = \boldsymbol{\nabla} \cdot \mathbf{F}_{\mathrm{SGS}}(\overline{\mathbf{w}}, \nabla \overline{\mathbf{w}}), \tag{8}$$

where $\overline{\mathbf{w}} = \left(\overline{\rho}, \overline{\rho}\widetilde{\mathbf{U}}, \overline{\rho}\widetilde{E}\right)^{\mathrm{T}}$ is the vector of filtered conservative variables.

The SGS tensor $\mathbf{F}_{\mathrm{SGS}}$ is the result of the filtering operation and it encapsulates the dynamics of the unresolved sub-grid scales, and is modeled here using the eddy-viscosity assumption:

$$\mathbf{F}_{\mathrm{SGS}}(\overline{\mathbf{w}}, \nabla \overline{\mathbf{w}}) = \begin{pmatrix} \mathbf{0} \\ 2\mu_t \overline{\mathbf{S}} \\ -\frac{\mu_t C_p}{Pr_t} \boldsymbol{\nabla} \widetilde{T}^{\mathrm{T}} \end{pmatrix}, \tag{9}$$

where $\overline{\mathbf{S}}$ is the shear stress tensor computed from equation (4) based on the Favre-filtered velocity $\widetilde{\mathbf{U}}$, Pr_t is the turbulent Prandtl number, which is set to 0.5,[13] C_p is the heat capacity at constant pressure of the fluid and μ_t is the eddy-viscosity which depends on the chosen sub-grid model.

In the present work, the CvP-Smagorinsky closure is adopted, which yields accurate results for transitional and high-Reynolds number flows.[1] The eddy viscosity for this closure reads:

$$\mu_t = \rho f(\sigma)(C_{\mathrm{S}}\overline{\Delta})^2\sqrt{S_{ij}S_{ij}} \tag{10}$$

where $C_{\mathrm{S}} = 0.172$ is the Smagorinsky constant, $\overline{\Delta}$ is the grid size and $f(\sigma)$ is the CvP turbulence sensor built from the ratio σ of test-filtered to grid-filtered enstrophy. This sensor attenuates the intensity of SGS dissipation of transitional turbulence or coherent vortices.

B. Numerical method

The compressible, Favre-filtered Navier-Stokes equations are solved using a 6th order compact finite difference scheme solver originally written by Nagarajan *et al.*,[14] currently under development at Purdue University. The solver is based on a staggered grid arrangement, providing superior accuracy compared to a fully collocated approach.[15] The speed of sound is adjusted so that the local Mach number does not exceed 0.1 for the computations performed in the present study, effectively simulating near incompressible flow dynamics. The time integration is performed using a third order Runge-Kutta scheme.

III. Problem Formulation

Simulations are performed in a cubic computational domain $\Omega = [0, 4R]^3$, where $R = 0.125$. The vortex ring is initialized at the center of the domain. Its vortex core radius is $r_c/R = 0.1$ and its circulation is $\Gamma = 0.01$. The Reynolds number based on the circulation is defined as $Re_\Gamma = \Gamma/\nu$, where ν is the kinematic viscosity. Grid size is refined for increasing Re_Γ, leading to the definition of 5-10 points inside the vortex core. The LES model considered is the CvP approach[1] which has been found to be successful for the prediction of transitional flows on coarse grids. A non-dimensional time $t^* = t\,\Gamma/R^2$ is considered for the study, where t is the flow time.

In this section, different perturbations are set up for the numerical study of vortex rings. The original vortex ring filament is initialized in a periodic, cubic box. The filament equation reads:

$$\mathbf{X}(\theta) = [R\cos(\theta), 0, R\sin(\theta)] \tag{11}$$

where R is the radius of the ring. Different levels of sinusoidal perturbation are added to the original path as described in Table 1, where $\overline{A}$ is the amplitude and n is the number of wavelengths along the ring circumference, related to the wavenumber via $n = kR$. Case A and B are initialized with a single mode corresponding to $n = 10$, as in Fig. 1(a), while Case C is defined with the sum of a set of N Fourier modes (here N= 12).A_n is a random variables which values are in $[-1, 1]$ and the absolute value of B_n is calculated according to $A_n^2 + B_n^2 = 1$, with its sign generated randomly. Thus the amplitude of each mode is 1 and a random phase can be obtained. To avoid a potential nonphysical perturbation, the final amplitude is confined to $0.1R \sim 0.2R$, as in Fig. 1(b). All perturbation angles are set to 45 degrees with respect to the propagation direction described in Fig. 1(c).

$$\mathbf{X_c}(\theta) = \mathbf{X_c}(\theta)[1 + \overline{A}f(\theta)] \tag{12}$$

$$f(\theta) = \sum_{n=1}^{N} A_n sin(n\theta) + B_n cos(n\theta) \tag{13}$$

case letter	mode(n)	amplitude $\overline{A}$	θ (degrees)	color code
(A)	10	$0.1R$	45	red
(B)	10	$0.2R$	45	blue
(C)	1∼12	$0.1R \sim 0.2R$	45	black

Table 1. Summary of test cases: $\overline{A}$: initial perturbation with different amplitudes, n: number of waves on the circumference

case number	Re_Γ	grid size	symbol
(I)	7,000	192^3	∘
(II)	70,000	288^3	□
(III)	700,000	384^3	△

Table 2. Reynolds number, grid size and symbol for each perturbation form

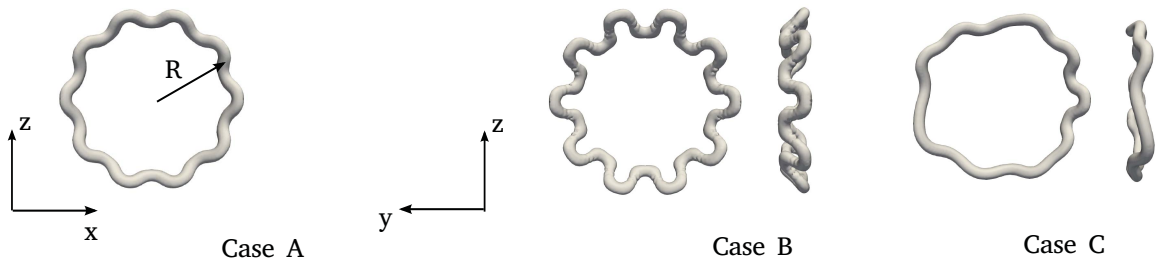

Figure 1. Sketch of the initial condition and parameters for the presently considered numerical setup.

The velocity field induced by the vortex filament is determined by the Biot-Savart law.

$$\mathbf{u}(\mathbf{x}) = -\frac{\Gamma}{4\pi}\int K_v \frac{(\mathbf{x}-\mathbf{X}(\theta))\times\mathbf{t}(\theta)}{|\mathbf{x}-\mathbf{X}(\theta)|^3}d\theta \tag{14}$$

where $\mathbf{t}(\theta)$ is the tangent vector to the helical filament, Γ is the circulation and K_v is a function allowing to define the shape of the vortex core[16] and reads:

$$K_v = \frac{|\mathbf{x}-\mathbf{X}(\theta)|^3}{\left(|\mathbf{x}-\mathbf{X}(\theta)|^{2k}+r_c^{2k}\right)^{\frac{3}{2k}}} \tag{15}$$

where $r_c = 0.05d$ is the core radius. The case $k = \infty$ corresponds to a Rankine vortex. The value of $k = 4$ is adopted to achieve a smooth transition between the inner, rotational flow and the outer, potential flow.

IV. Results

A. Stable case with low amplitude perturbation

In this section, we study the dynamics of the perturbed vortex rings.

For the cases with small initial perturbation (single mode) and low Reynolds number (case A,B-I), the general process of evolution can be shown in Figure 2, visualized by the iso-vorticity contours for various times corresponding to the generation of the secondary structure.

Those structures consist in pairs of counter-rotating vortices, namely dipoles, generated at the crests and peaks of the initial perturbation shortly after the beginning of the simulation ($t^* = 0.32$). The dipoles wrap around the vortex ring as the original perturbation is smeared out. At $t^* = 1.28$ the original pattern is restored and the dipole structures becomes stable, then the vortex ring keeps flattening due to diffusion. The dipoles quickly dissipate and the growth of a higher mode with respect to the original perturbation is detected ($t^* = 12.8$).

Case B-I exhibits a similar pattern with more intense evolution, in which reconnection happens at the tail and head of dipoles as in Figure 3(a). These structures are described as hairpin vortices ejected from the vortex ring by Archer et al.[17 18] , but the present study suggests that these structures are rather the product of reconnection of dipoles, which are the real structures ejected.

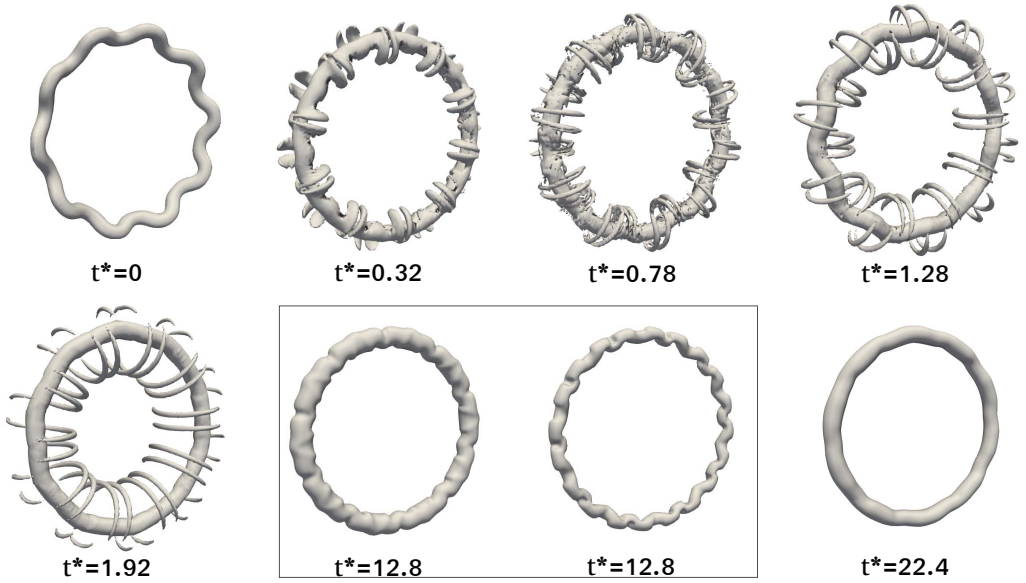

Figure 2. The Q-criterion contours (The threshold is set to yield the best visualization at $Q\Gamma^4R^{-6}$=1907) of Case A-I for various times corresponding to the evolution of the vortex ring with initial perturbation. Plots of $t^* = 12.8$ in box are generated with different Q iso-surfaces (left :$Q\Gamma^4R^{-6}$=1907,right:$Q\Gamma^4R^{-6}$=3814).

The reconnection also happens for higher Reynolds number case (A-I, A-III, B-II, B-III) and higher amplitude perturbation (B-I). For higher Reynolds number cases, the reconnection along anti-parallel lines also happens with the same dynamics shown in Figure 3(b).

B. Unstable case with high amplitude perturbation

Vortex breakdown in the sense of rupture of continuity of the main vortex line is only detected in Cases B-II and B-III, where the vortex evolution is totally different from others. Figure 4 shows two Q iso-surfaces with distinct levels: $Q\Gamma^4R^{-6}$=76300 indicated in red; $Q\Gamma^4R^{-6}$=7630 in transparent blue. Dipoles begin to develop at the beginning of the simulation and the intensity of core decrease due to the ejection ($t^* = 0.32$). When dipoles become stable, the core region reorganizes itself in a seemingly coherent single vortex but with isolated discontinuities. The intensity of core region increases up to $t^* = 1.28$, at which point breakdown occurs and core region regenerates into a collection of multiple vortex threads. At $t^* = 2.56$, the vortex core is almost dissipated and ejected dipoles show higher intensity. At $t^* = 3.52$, the Q-isosurface with high values (red) cannot detect the vortex core, with

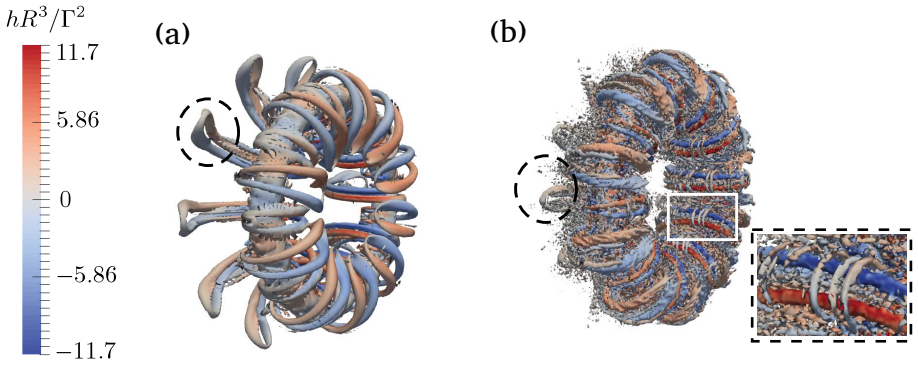

Figure 3. Different types of reconnection among dipoles. (a)the reconnection takes place at the tail and head (Case B-I,$t^* = 1.92$, $Q\Gamma^4R^{-6}$=191) (b) reconnection along anti-parallel vortex lines (Case A-I,$t^* = 1.58$, $Q\Gamma^4R^{-6}$=191)

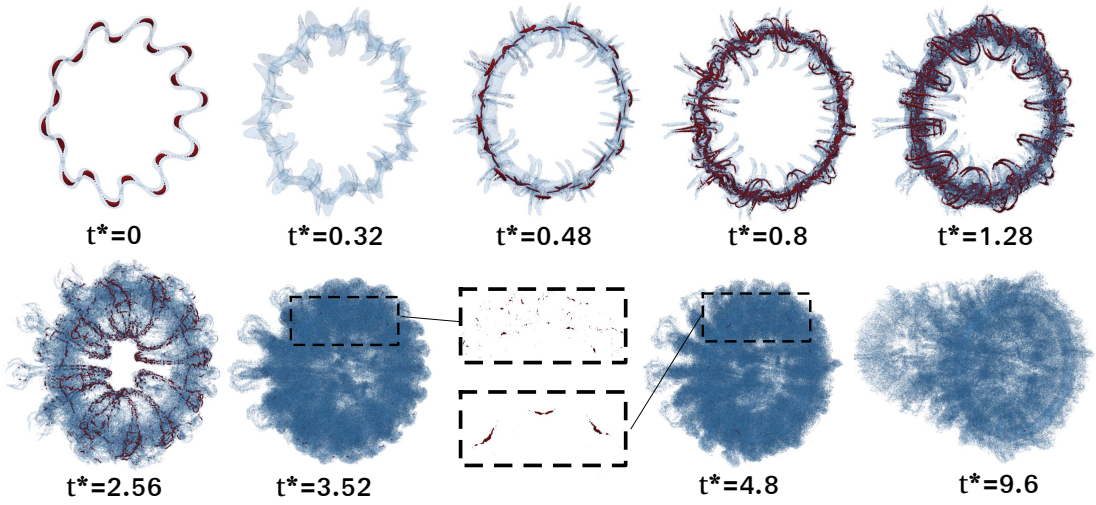

Figure 4. Vortex breakdown of Case B-III. Red solid surface: $Q\Gamma^4R^{-6}$=76300; blue transparent surface: $Q\Gamma^4R^{-6}$=7630

the exception of a few isolated strands; yet at $t^* = 4.8$, a concentration of vorticity on the vortex core is captured again, although weak and only present on the crest part of original perturbation. $t^* = 9.6$ shows the final status, similarly to what happens for the low amplitude cases, the vortex ring keeps traveling with secondary structures dissipating gradually.

The enstrophy is defined as $\xi = \omega \cdot \omega/2$, where ω is the vorticity vector. This quantity is sensitive to the dynamics of the small scales in the flow as these carry a significant amount of vorticity. The temporal evolution of volume-averaged enstrophy is shown in Figure 5, from where bursting can also be observed . The peak at $t^* = 2.6$ is clearly correlated to Figure 4. On one hand, the peak may represent the most intense small scale structures during/after bursting; on the other hand, it may result form the interaction of anti-parallel dipoles. The contact of dipoles is only detected in Case B-II and B-III, which results from the initial perturbation. A plateau can be observed in the evolution of enstrophy for Case B and Case C, which means the small scales can be sustained for a long time, and have not begun to dissipate in current simulations.

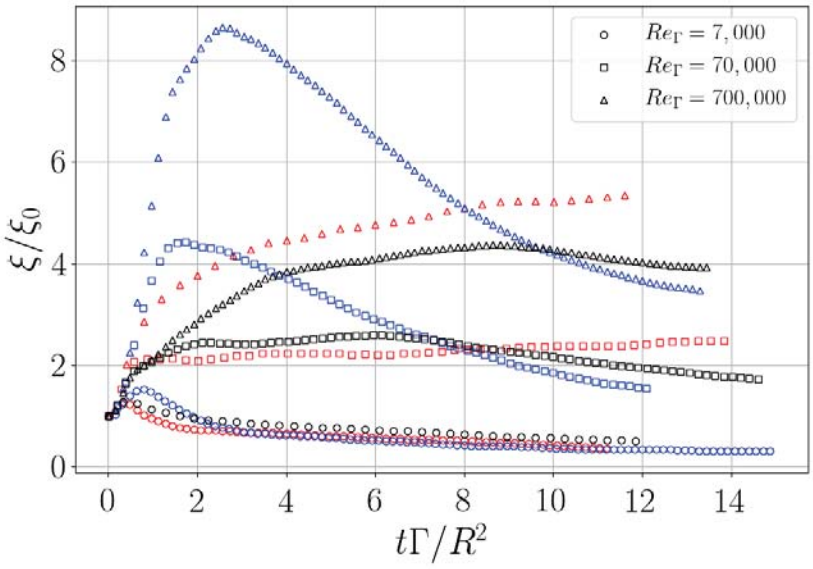

Figure 5. Evolution of enstrophy. Red: Case A, small amplitude; Blue: Case B, large amplitude; Black: Case C, multiple modes

C. Persistence of coherent structures

One-dimensional energy spectra are computed at $t^* = 12.8$ (final state in current simulations) in the vortex propagation direction $-y$ and averaged in $x-z$ planes and shown in Figure 7. A $-5/3$ slope can only be observed at $Re_\Gamma = 700,000$. Two regions of energy transfer can be observed, which may result from the inhomogeneity of turbulence. For all Reynolds numbers, the energy of Case B is always lower than Case A and Case C, which results from the intense energy dissipation occuring during the bursting process. A bump is observed at $Re_\Gamma = 7,000$, which evolves in time and the number of bumps increases as well. This mechanism has yet to be explained in future studies.

Case (B-I) does not experiences the bursting process, but also shows lower vorticity magnitude in comparison with A-I and B-I. This perhaps results from the difference in initial velocity field. The large displacement of the vortex line in the y direction behaves like anti-parallel vortex tubes, which undergo viscous cancellation, especially for higher perturbation amplitudes (Case B). The induced velocity is canceled in Case B more than in Case A, even if the circulation is the same in both cases. Since the structures of the perturbation are asymmetric in Case C, the interaction region of the anti-parallel tubes is smaller than Case A and B. This means that the initial flow field of Case C is slightly stronger than in Case A and B, and therefore results in higher vorticity even after a period of decay via viscous dissipation.

Another possible explanation can be proposed through the study of the helicity, or the helicity density h, which is defined as $h = \mathbf{u} \cdot \mathbf{w}$, where $\mathbf{u}$ is the velocity vector and $\mathbf{w} = \nabla \times \mathbf{u}$ is the vorticity vector. Hussain[19] has proposed that the helicity h can inhibit the Kolmogorov cascade. According to the trigonometric identity Eq. 16, wherever $\mathbf{u} \cdot \mathbf{w}$ is large, $\mathbf{u} \times \mathbf{w}$ is small for given amplitude of $\mathbf{u}$ and $\mathbf{w}$. The nonlinear term $\mathbf{u} \times \mathbf{w}$ in the momentum equation Eq. 17 is one of the terms responsible for the cascade from larger to smaller scales. Thus high helicity regions are expected to display lower dissipation levels and therefore to persist longer. This perhaps explains why dipoles, showing high helicity, can persist for a long time along the vortex ring.

$$|\mathbf{u} \cdot \mathbf{w}|^2 + |\mathbf{u} \times \mathbf{w}|^2 = |\mathbf{u}|^2 |\mathbf{w}|^2 \tag{16}$$

$$\frac{\partial \mathbf{u}}{\partial t} = -\mathbf{u} \times \mathbf{w} - \nabla(\frac{p}{\rho} + \frac{\mathbf{u}^2}{2}) + \nu \nabla^2 \mathbf{u} \tag{17}$$

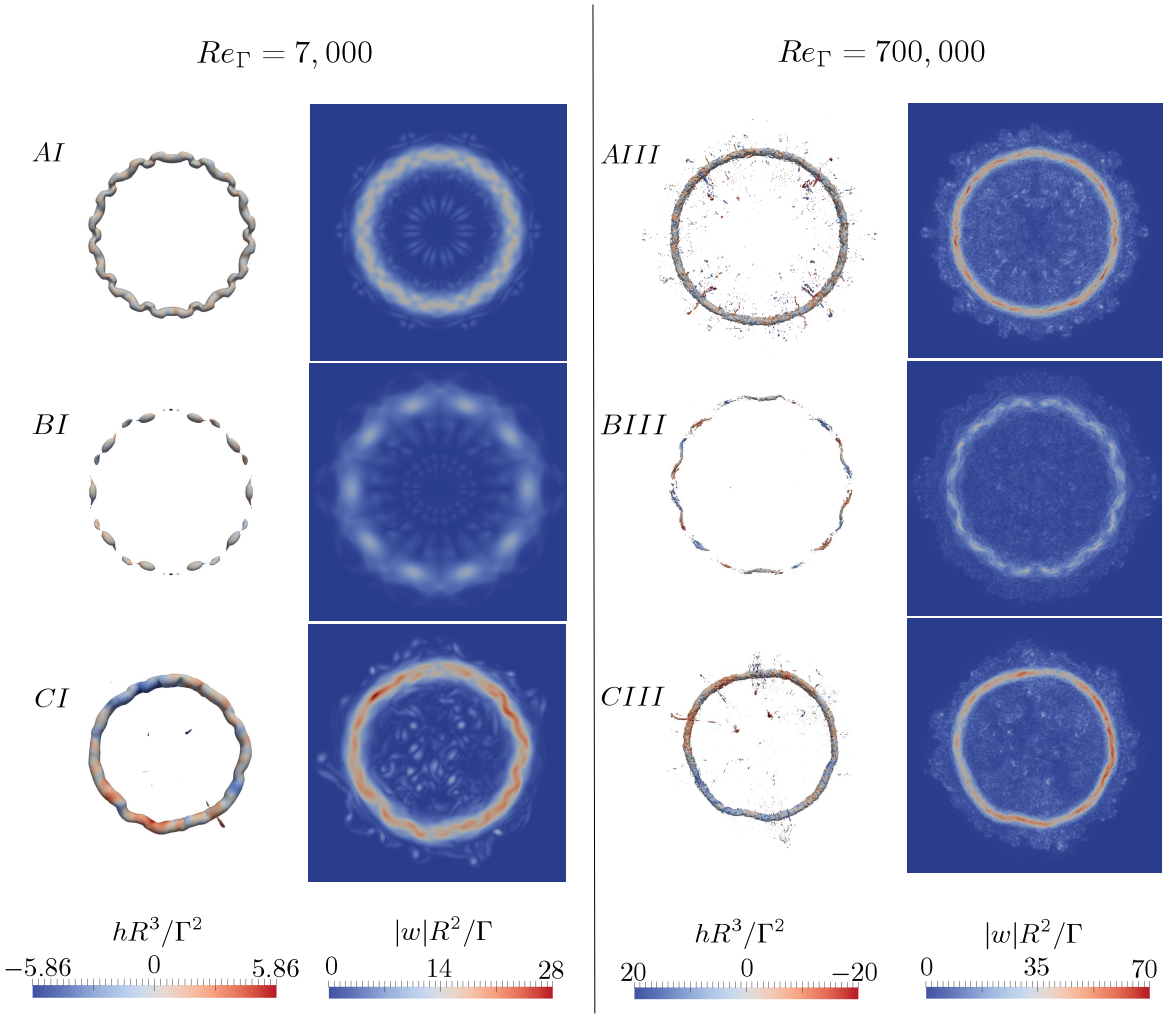

Figure 6. Iso-surfaces of Q-criterion and vorticity magnitude contours at $t^* = 12.8$ showing final status of evolution. Left: $Re_\Gamma = 7,000$ visualized by $Q\Gamma^4 R^{-6}$=5700 right: $Re_\Gamma = 700,000$ with $Q\Gamma^4 R^{-6}$=30500.

D. Axial flow

The helicity contains information regarding the angle between vectors **u** and **w**. For vortex ring, high helicity implies the presence of axial flow, the flow directed along the vortex line. A weak axial flow is observed in all cases, and is only local in Cases A and B, as shown in Figure 6. Intense axial flow generates due to the non-uniform distribution of perturbation in Case C.

The generation of axial flow is explained in Figure 8; a slice cut of the vortex ring at the left cross-section shows a flattening of the structure compared to the right cross section in the crest of waves. Helicity exists initially on both sides of vortex tube, as can be seen in Figure 8(a), with opposite signs but respecting symmetry. Vortex sheets quickly roll up in multiple layers while the axial flow is not increasing as seen in Figure 8(b). At the same time the high wavenumber region begins to develop dipoles in Case A and B, the contour of which shows reduced layers because of the wider influence

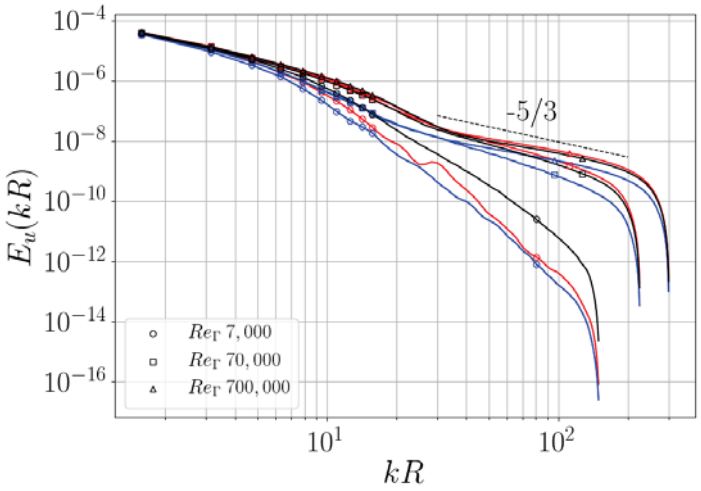

Figure 7. 1D energy spectra computed at $t^* = 12.8$ in the vortex propagation direction y and averaged in planes $x - z$. Red: Case A, small amplitude; Blue: Case B, large amplitude; Black: Case C, multiple modes

region of dipoles . In Figure 8(c), the flattened part still sustains symmetry while the contour near dipoles shows stronger negative helicity. This results to the ejection of the dipoles from the original vortex ring, which leads to lower vorticity and thus higher pressure in the vortex core. The pressure gradient drives a downward axial flow. While the axial vorticity goes counter-clockwise in this view, a dominant negative helicity can be observed. In Figure 8(d), the asymmetric right cross section restores the symmetry because of the generation of dipoles on the other side of the plane. Therefore we can conclude that the axial flow is excited by the pressure gradient inside the vortex core, resulting from the ejection of dipoles. Dipoles region ,i.e. high curvature part generates axial flow in opposite direction and then the high wavenumber part cancels such axial flow in a symmetric way so the helicity can only be observed locally, as shown in Figure 6(B-III). The flattened part allows for the development of axial flow and traveling of helical structures .

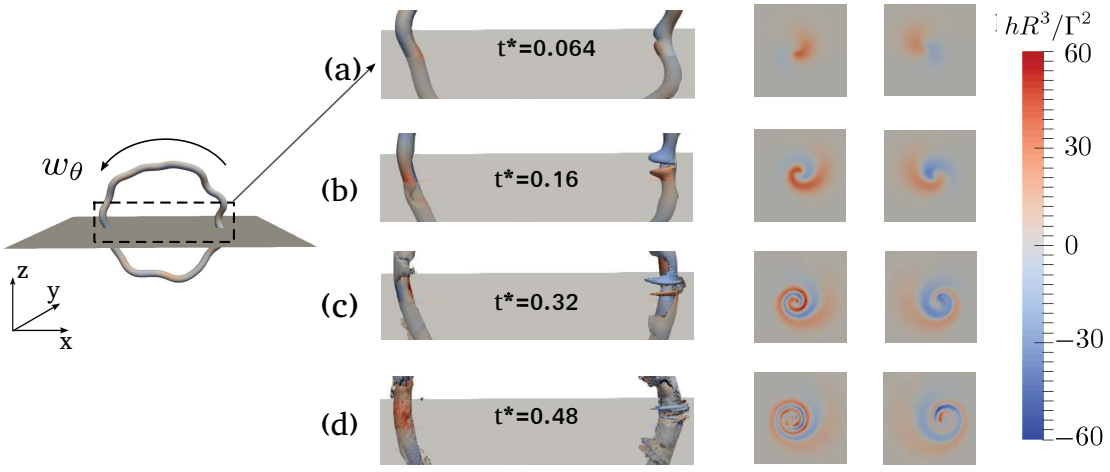

Figure 8. Generation of initial axial flow. From top to bottom, $t^* = 0.064, 0.16, 0.32, 0.48$. Both vortex ring and slices are colored by helicity.

The developed axial flow travels along the vortex ring in both direction. The helical mode is

activated and helical structures can be observed in Figure 9(a). Figure 9 shows the process of two helical structures colliding and then passing by. Figure 9(a) shows the cross section of two helical structures with opposite sign traveling with opposite z direction velocity. When colliding, the vortex iso-surface is largely diffused and no clear z direction velocity can be captured as in Figure 9(b). At the same time, some parts of the helical structure have finished collision process and keep traveling, and are defined as the "passing by" part. Figure 9(c) shows the end of this collision, with the helicity intensity slightly decreased. Yet since the traveling happens on the vortex loop, this kind of collision will keep happening. Figure 9 only shows one collision on the vortex ring at this moment, yet in fact several collisions can happen at the same time at different locations of ring.

The effect of such collisions is still largely unexplored. Future investigations will focus on explaining how persisting coherent helical structures stabilize the flow field, beyond the canceling velocity observation.

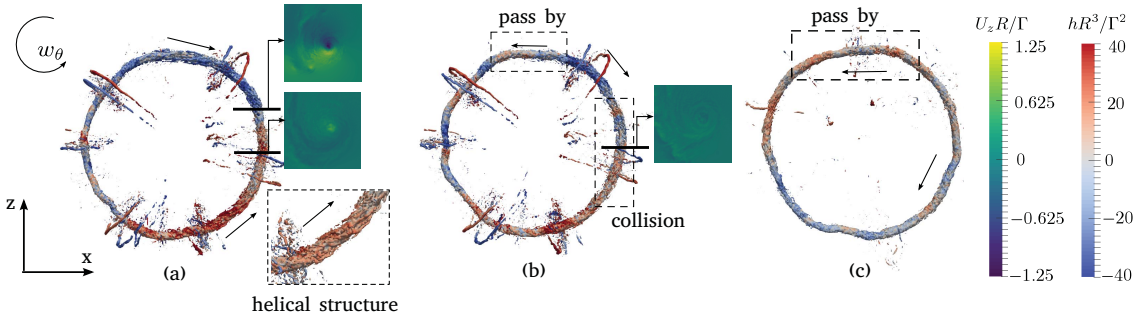

Figure 9. Helical structures keep traveling along vortex ring and colliding. From left to right, $t^* = 4.48, 4.8, 5.12$. Vortex ring is colored by helicity while slice show z direction velocity.

V. Conclusion

In this work, the dynamics of vortex rings subject to large perturbations were studied by the means of state-of-the-art LES computations. The numerical simulations of the vortex ring shows dissipation and bursting processes in which secondary vortex structures are generated and developed.

Bursting process is only observed at high Reynolds number, and happens at the beginning of simulations, together with an intense generation of secondary dipoles. The initial Vortex core loses its original coherence and can only be visualized by multiple vortex threads, which dissipate faster than dipoles. At the end of the simulation the core region shows a weakly restored coherence.

Three different types of perturbation show completely different evolution processes. The final states of the present simulations are compared, and the explanation of persistent structures is believed to be either the energy difference in initial velocity field or the reverse on energy cascade of helicity.

An important axial flow is observed for non-uniform perturbation cases. Helical instability develops and generates helical structures which travel along the vortex ring, and collide yielding a slight decrease in helicity, then keep crossing and traveling. The effect of the helicity and the collision is still unclear and will be the topic of future investigations.

VI. Acknowledgements

The authors acknowledge the support of the Army Research Office's Young Investigator Program (ARO-YIP) Award W911NF-18-1-0045 for the proposal entitled: "Coherent-vorticity-Preserving (CvP) Large-Eddy Simulations (LES) of Very-High-Reynolds-Number Vortex Dynamics".

References

[1]Chapelier, J.-B., Wasistho, B., and Scalo, C., "A Coherent vorticity preserving eddy-viscosity correction for Large-Eddy Simulation," *Journal of Computational Physics*, Vol. 359, 2018, pp. 164 – 182.

[2]Widnall, S. E. and Sullivan, J. P., "On the Stability of Vortex Rings," *Proceedings of the Royal Society A Mathematical Physical & Engineering Sciences*, Vol. 332, No. 332, 1973, pp. 335–353.

[3]Widnall, S. E., Bliss, D. B., and Tsai, C.-Y., "The instability of short waves on a vortex ring," *Journal of Fluid Mechanics*, Vol. 66, No. 1, 1974, pp. 35 – 47.

[4]Shariff, K., Verzicco, R., and Orlandi, P., "A numerical study of three-dimensional vortex ring instabilities: viscous corrections and early nonlinear stage," *Journal of Fluid Mechanics*, Vol. 279, No. 279, 2006, pp. 351–375.

[5]Dazin, A., Dupont, P., and Stanislas, M., "Experimental characterization of the instability of the vortex ring. Part I: Linear phase," *Experiments in Fluids*, Vol. 40, No. 3, 2006, pp. 383.

[6]Dazin, A., Dupont, P., and Stanislas, M., "Experimental characterization of the instability of the vortex rings. Part II: Non-linear phase," *Experiments in Fluids*, Vol. 41, Sept. 2006, pp. 401–413.

[7]BergdorfM, KoumoutsakosP, and LeonardA, "Direct numerical simulations of vortex rings at $Re_\Gamma = 7500$," *Journal of Fluid Mechanics*, Vol. 581, No. 4, 2007, pp. 495–505.

[8]Leonard, A., "Energy cascade in large-eddy simulations of turbulent fluid flows," *Adv. Geophys.*, Vol. 18, 1974, pp. 237–248.

[9]Sagaut, P., *Large-Eddy simulation for incompressible flows: an introduction*, Springer Verlag, 2006.

[10]Lesieur, M. and Comte, P., "Favre filtering and macro-temperature in Large-Eddy simulations of compressible turbulence," *CR. Acad. Sci. Serie II*, Vol. 329, No. 5, 2001, pp. 363–368.

[11]Lesieur, M., Métais, O., and Comte, P., *Large-Eddy simulations of turbulence*, Cambridge University Press, 2005.

[12]Lesieur, M. and Metais, O., "New trends in Large-Eddy simulations of turbulence," *Ann. Rev. Fluid Mech.*, Vol. 28, No. 1, 1996, pp. 45–82.

[13]Erlebacher, G., Hussaini, M., Speziale, C., and Zang, T., "Toward the Large-Eddy simulation of compressible turbulent flows," *J. Fluid Mech.*, Vol. 238, No. 1, 1992, pp. 155–185.

[14]Nagarajan, S., Lele, S., and Ferziger, J., "A robust high-order compact method for large eddy simulation," *Journal of Computational Physics*, Vol. 191, 2003, pp. 392–419.

[15]Lele, S., "Compact finite difference schemes with spectral-like resolution," *Journal of Computational Physics*, Vol. 103, No. 1, 1992, pp. 16–42.

[16]Bagai, A. and Leishman, J. G., "Flow visualization of compressible vortex structures using density gradient techniques," *Experiments in Fluids*, Vol. 15, 1993, pp. 431–442.

[17]Archer, P. J., Thomas, T. G., and Coleman, G. N., "Direct numerical simulation of vortex ring evolution from the laminar to the early turbulent regime," *Journal of Fluid Mechanics*, Vol. 598, 2008, pp. 201–226.

[18]Weigand, A. and Gharib, M., "On the decay of a turbulent vortex ring," *Physics of Fluids - PHYS FLUIDS*, Vol. 6, 12 1994, pp. 3806–3808.

[19]Hussain, A. K. M. F., "Coherent structures and turbulence," *Journal of Fluid Mechanics*, Vol. 173, 1986, pp. 303–356.